Naval Research Laboratory

Washington, DC 20375-5320

NRL/MR/6790--13-9496

Numerical Relativistic Quantum Optics

D.F. Gordon
B. Hafizi
M.H. Helle

Beam Physics Branch
Plasma Physics Division

November 8, 2013

Approved for public release; distribution is unlimited.

REPORT DOCUMENTATION PAGE

Form Approved
OMB No. 0704-0188

Public reporting burden for this collection of information is estimated to average 1 hour per response, including the time for reviewing instructions, searching existing data sources, gathering and maintaining the data needed, and completing and reviewing this collection of information. Send comments regarding this burden estimate or any other aspect of this collection of information, including suggestions for reducing this burden to Department of Defense, Washington Headquarters Services, Directorate for Information Operations and Reports (0704-0188), 1215 Jefferson Davis Highway, Suite 1204, Arlington, VA 22202-4302. Respondents should be aware that notwithstanding any other provision of law, no person shall be subject to any penalty for failing to comply with a collection of information if it does not display a currently valid OMB control number. *PLEASE DO NOT RETURN YOUR FORM TO THE ABOVE ADDRESS.*

1. REPORT DATE *(DD-MM-YYYY)*	**2. REPORT TYPE**	**3. DATES COVERED** *(From - To)*
08-11-2013	Interim	October 2012 – September 2013

4. TITLE AND SUBTITLE

Numerical Relativistic Quantum Optics

5a. CONTRACT NUMBER

5b. GRANT NUMBER

5c. PROGRAM ELEMENT NUMBER

6. AUTHOR(S)

D.F. Gordon, B. Hafizi, and M.H. Helle

5d. PROJECT NUMBER
67-4660-04

5e. TASK NUMBER

5f. WORK UNIT NUMBER

7. PERFORMING ORGANIZATION NAME(S) AND ADDRESS(ES)

Naval Research Laboratory
4555 Overlook Avenue, SW
Washington, DC 20375-5320

8. PERFORMING ORGANIZATION REPORT NUMBER

NRL/MR/6790--13-9496

9. SPONSORING / MONITORING AGENCY NAME(S) AND ADDRESS(ES)

Naval Research Laboratory
4555 Overlook Avenue, SW
Washington, DC 20375-5320

10. SPONSOR / MONITOR'S ACRONYM(S)

NRL

11. SPONSOR / MONITOR'S REPORT NUMBER(S)

12. DISTRIBUTION / AVAILABILITY STATEMENT

Approved for public release; distribution is unlimited.

13. SUPPLEMENTARY NOTES

14. ABSTRACT

A general solution for relativistic quantum optics problems is developed, with a view toward describing the ionization of high charge state ions by laser fields. Solutions of the Dirac and Klein-Gordon equations are discussed, with emphasis on the latter. The stationary states in a Coulomb potential and uniform magnetic field are determined analytically and numerically. Fully time dependent numerical calculations of relativistic wavefunctions in extreme magnetic fields are validated. The relativistic ionization rate is computed for an ion illuminated by a laser field near the usual barrier suppression threshold, which, so far, appears to remain valid in the relativistic limit. Ponderomotive effects can be seen in the calculated wavefunction. Computational performance is important due to the rapid oscillations in a relativistic wavefunction. Multiple General Purpose Graphical Processing Units are utilized in parallel by means of the Message Passing Interface in order to speed up calculations.

15. SUBJECT TERMS

Photoionization GPGPU Extreme fields
Relativistic Klein-Gordon

16. SECURITY CLASSIFICATION OF:			**17. LIMITATION OF ABSTRACT**	**18. NUMBER OF PAGES**	**19a. NAME OF RESPONSIBLE PERSON**
					Daniel F. Gordon
a. REPORT	**b. ABSTRACT**	**c. THIS PAGE**	Unclassified Unlimited	27	**19b. TELEPHONE NUMBER** *(include area code)*
Unclassified Unlimited	Unclassified Unlimited	Unclassified Unlimited			(202) 767-5036

Standard Form 298 (Rev. 8-98)
Prescribed by ANSI Std. Z39.18

Numerical Relativistic Quantum Optics

D.F. Gordon, B. Hafizi, and M.H. Helle

Beam Physics Branch, Plasma Physics Division

A general solution for relativistic quantum optics problems is developed, with a view toward describing the ionization of high charge state ions by laser fields. Solutions of the Dirac and Klein-Gordon equations are discussed, with emphasis on the latter. The stationary states in a Coulomb potential and uniform magnetic field are determined analytically and numerically. Fully time dependent numerical calculations of relativistic wavefunctions in extreme magnetic fields are validated. The relativistic ionization rate is computed for an ion illuminated by a laser field near the usual barrier suppression threshold, which, so far, appears to remain valid in the relativistic limit. Ponderomotive effects can be seen in the calculated wavefunction. Computational performance is important due to the rapid oscillations in a relativistic wavefunction. Multiple General Purpose Graphical Processing Units are utilized in parallel by means of the Message Passing Interface in order to speed up calculations.

Manuscript Approved October 11, 2013

Contents

I. Introduction 1

II. Relativistic Wave Equations 2

III. Stationary States 4

A. Analytical Solutions for Coulomb Potentials 4

B. Numerical Solutions for Soft Core Potentials 6

C. Scalar Zeeman Effect 7

IV. Time Dependent Simulations 10

A. Numerical Algorithm 10

B. Validation Against Zeeman Effect 12

C. Relativistic Ionization Example 15

V. Computational Performance 18

VI. Conclusions 21

VII. Acknowledgements 22

References 23

I. INTRODUCTION

Tunneling ionization is usually described using the time dependent Schrödinger equation (TDSE). The TDSE is a strictly non-relativistic equation. In contrast, the dynamics of a free particle become relativistic when the normalized vector potential, $a = eA/mc^2$, satisfies $a \gtrsim 1$. For typical laser frequencies, this corresponds to an irradiance $I \approx 10^{18}$ W/cm^2. Such irradiances are achieved regularly in many laboratories. The corresponding fields are sufficient to strip nitrogen down to the K-shell via barrier suppression. Irradiances of $I > 10^{20}$ W/cm^2 are not achieved as frequently, but are easily within the reach of several ultra-high power laser systems around the world. It is expected that these irradiances are sufficient to fully strip neon.

Although the dynamics of free electrons are relativistic for $a \gtrsim 1$, the spectra of atoms that can be brought to a high charge state by such a field are non-relativistic. Put another way, all the bound electrons in an atom that requires $a \gtrsim 1$ to be fully stripped, are well described by Schrödinger theory. To see this, note that for a hydrogen-like ion, the barrier suppression model [1] gives the threshold for ionization as

$$a = \frac{\alpha}{\omega_L \tau_a} \frac{Z^3}{16} \tag{1}$$

where Z is the atomic number, ω_L is the laser frequency, $\tau_a = \hbar^3/me^4$ is the atomic unit of time, and $\alpha = e^2/\hbar c$ is the fine structure constant. Taking $a = 1$ and a laser wavelength $\lambda = 0.8$ μm ($\omega_L \tau_a = 0.057$) gives $Z = 5$. Hence, boron is the heaviest element that is fully stripped by a laser with $\lambda = 0.8$ μm and $a = 1$. The condition for an atomic spectrum to be non-relativistic is $Z \ll \alpha^{-1} \approx 137$, as follows from elementary Dirac theory. One concludes that even though $a = 1$ leads to relativistic motion of free electrons, the bound electrons that are freed are non-relativistic. This observation can be useful when formulating the initial conditions for a relativistic quantum optics problem.

The process of ionization involves the dynamics of both bound and free electrons. For $a \gtrsim 1$ and $Z \ll 137$, the bound electrons are quantum mechanical and non-relativistic, while the free electrons are relativistic and classical. If much heavier elements are considered, even the bound electrons might have to be treated relativistically. Hence, a complete description of the problem must be quantum mechanical and fully relativistic. In this report we develop a numerical tool capable of treating such problems.

TABLE I: Natural Units

Quantity	Unit	SI Value
Velocity	c	2.9979×10^{8} m/s
Charge	$\lvert q_e \rvert / \alpha^{1/2}$	1.8755×10^{-18} C
Mass	m_e	9.1094×10^{-31} kg
Length	$\hbar / m_e c$	3.8616×10^{-13} m
Time	$\hbar / m_e c^2$	1.2881×10^{-21} s
Angular Momentum	$\hbar$	1.0546×10^{-34} J·s

The non-relativistic theory of photo-ionization was pioneered by L.V. Keldysh in 1965 [2]. Shortly thereafter, in the series of papers by Perelemov et al. [3–6], it was brought into a form that has remained useful right up to the present day. Relativistic photo-ionization has received less attention, although some analyses have been given [7–9]. Fully time dependent numerical solutions of relativistic wave equations are only recently appearing in the literature [10, 11].

II. RELATIVISTIC WAVE EQUATIONS

The Dirac equation describes the motion of an electron in an external potential, such as the superposition of an atomic binding potential and a laser field. Solution of the Dirac equation requires evolving a 4-component bi-spinor wavefunction. However, as discussed in Ref. [12], the Dirac equation can be separated into 4 independent equations by neglecting terms involving spin. This results in the Klein-Gordon equation

$$\left[(\imath \partial_t + q\Phi)^2 - (\imath \nabla + q\mathbf{A})^2 - m^2 \right] \Psi = 0 \tag{2}$$

where q is the charge and m is the mass of the particle. Here, and in all that follows, natural units are employed (see Table I). Using the Coulomb gauge, $\nabla \cdot \mathbf{A} = 0$, and assuming a static scalar potential,

$$\left(\Box^2 - m^2 + q^2 A_\mu A^\mu \right) \Psi + 2\imath q \partial_\mu (A^\mu \Psi) = 0 \tag{3}$$

where $\Box^2 = \nabla^2 - \partial_t^2$, μ is a relativistic tensor index, and the metric signature is $(+ - - -)$. Note that in the chosen gauge $\nabla \cdot (\mathbf{A}\Psi) = \mathbf{A} \cdot \nabla \Psi$. The expression on the left is useful for

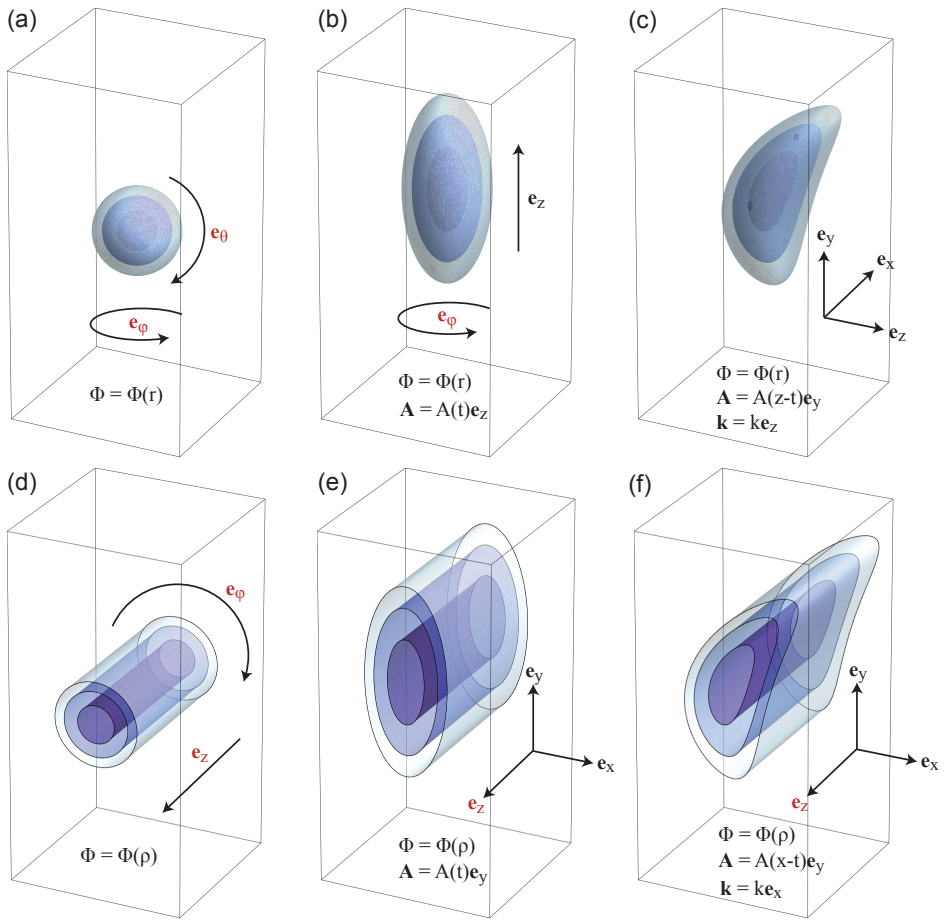

FIG. 1: Cartoon of an atomic wavefunction in various scenarios. (a) bound state, (b) non-relativistic ionizing state, (c) relativistic ionizing state, (d) cylindrical bound state, (e) cylindrical non-relativistic ionizing state, (f) cylindrical relativistic ionizing state. Coordinate axes are labeled by basis vectors taken from any of the Cartesian, cylindrical, or spherical coordinates, with ignorable coordinates in red.

finite volume differencing, while the one on the right is useful for analysis.

Depending on the problem, various coordinate systems are used to solve Eq. (3). In this report Cartesian coordinates (x, y, z), cylindrical coordinates (ρ, φ, z), and spherical coordinates (r, θ, φ) are used. Cartoons of various wavefunctions are shown in Fig. 1. Panels (a), (b), and (c) are for a central binding potential $\Phi(r)$, while (d), (e), and (f) are for a cylindrical binding potential $\Phi(\rho)$. Naturally, the former case is a more realistic model of an atom or ion. Panels (a) and (d) show a bound state wavefunction for which $\mathbf{A} = 0$. In both geometries, two coordinates are ignorable. Panels (b) and (e) show an ionizing wavefunction

is the non-relativistic dipole approximation, where $\mathbf{A} = \mathbf{A}(t)$ is a function of time only. The effect of the vector potential is to stretch the wavefunction in the polarization direction. For a central potential, φ is ignorable, while for a cylindrical potential z is ignorable. Panels (c) and (f) show an ionizing wavefunction in the relativistic case, where the spatial dependence of $\mathbf{A}$ leads to a ponderomotive force that stretches the wavefunction in the direction of the photon momentum, $\mathbf{k}$. In this case, there is no coordinate that is ignorable for a central potential, but there is one that is ignorable for a cylindrical potential. This is the reason for considering a cylindrical potential.

III. STATIONARY STATES

A. Analytical Solutions for Coulomb Potentials

The time independent form of Eq. (3) is obtained by making the substitution $\Psi(\mathbf{r}, t) \to \psi(\mathbf{r}) \exp(-\imath\omega t)$. Using $\partial_t \Phi = 0$, this gives

$$\left(\nabla^2 - \omega^2 + 2q\Phi\omega + q^2 A_\mu A^\mu - m^2\right)\psi - 2\imath q \nabla \cdot (\mathbf{A}\psi) = 0 \tag{4}$$

Specializing to the case of a uniform magnetic field $\mathbf{A} = \frac{1}{2}\rho B_0 \mathbf{e}_\varphi$ gives

$$\left(\nabla^2 - \omega^2 + 2q\Phi\omega + q^2\Phi^2 + \ell_z q B_0 - \frac{1}{4}\rho^2 q^2 B_0^2 - m^2\right) R(\rho, z) = 0 \tag{5}$$

Here, the cylindrical coordinates are denoted (ρ, φ, z), and ℓ_z is the magnetic quantum number, defined such that

$$\psi(\mathbf{r}) = R(\rho, z) \exp(\imath \ell_z \varphi) \tag{6}$$

As discussed above, the use of cylindrical coordinates is motivated by the fact that for a cylindrical atom, one coordinate is ignorable even in the case of a fully relativistic problem. The effect of this fictitious geometry on the energy levels is determined below.

In the case of a Coulomb potential with $B_0 = 0$, the bound states can be determined exactly. Approximate solutions can be found for a weak magnetic field. Consider first a spherical potential, $\Phi = Q/r$, where $Q = Z\alpha^{1/2}$ is the charge of the nucleus (we are considering hydrogen-like ions). Then the bound state energies are

$$\omega = m\left(1 - \frac{\ell_z \omega_c}{m}\right)^{1/2}\left[1 + \frac{Q^2 q^2}{\left(n_r + \frac{1}{2} \pm \sqrt{(\ell + \frac{1}{2})^2 - Q^2 q^2}\right)^2}\right]^{-1/2} \tag{7}$$

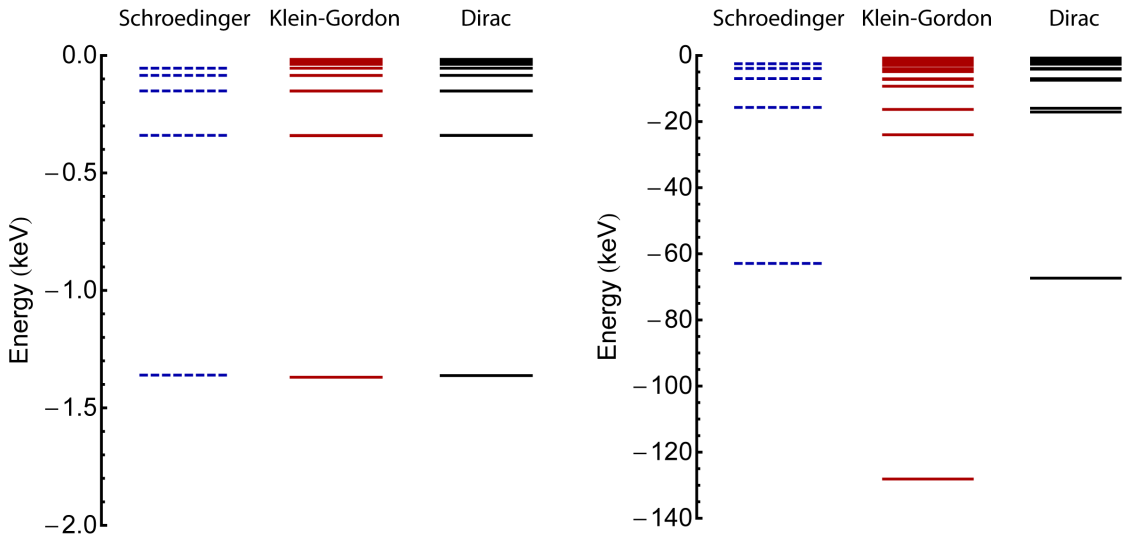

FIG. 2: Energy levels of spherical ions according to Schrödinger, Klein-Gordon, and Dirac theories, for (left) hydrogen-like neon and (right) hydrogen-like erbium. The magnetic field is zero.

where $\omega_c = qB_0/m$ is a signed cyclotron frequency, n_r is the radial quantum number and ℓ is the orbital quantum number. The principle quantum number is $n \equiv n_r + \ell + 1$, which completely determines the energy in the *non-relativistic* limit, if $B_0 = 0$. The radial eigenfunctions, to within a normalization factor, are

$$R(r) = F(-n_r, 2(a+1), 2kr) r^a e^{-kr} \tag{8}$$

where F is the confluent hypergeometric function, $a = -1/2 \pm \sqrt{(\ell+1/2)^2 - Q^2q^2}$, and $k = \sqrt{m^2 - \ell_z m\omega_c - \omega^2}$. The condition that the field should be weak reads $\sqrt{\omega_c} \ll k$.

A comparison of the energy levels predicted by Klein-Gordon theory, Schrödinger theory, and Dirac theory, is shown in Fig. 2. The levels shown are taken from the set $\{n_r \in 0,1,2,3,4\} \bigotimes \{\ell \in 0,1,2,3,4\}$. In the Schrödinger theory the energy depends only on the combination $n_r + \ell$. Note that for neon, the difference is subtle, whereas for erbium it is pronounced. For elements heavier than erbium, the square root in the expression for ω becomes imaginary, so that no stationary state exists for $\ell = 0$ and $Z > 68$.

For a cylindrical potential, $\Phi = Q/\rho$ [16], the bound state energies are

$$\omega = m\left(1 - \frac{\ell_z\omega_c}{m}\right)^{1/2}\left[1 + \frac{Q^2q^2}{\left(n_r + \frac{1}{2} \pm \sqrt{\ell_z^2 - Q^2q^2}\right)^2}\right]^{-1/2} \tag{9}$$

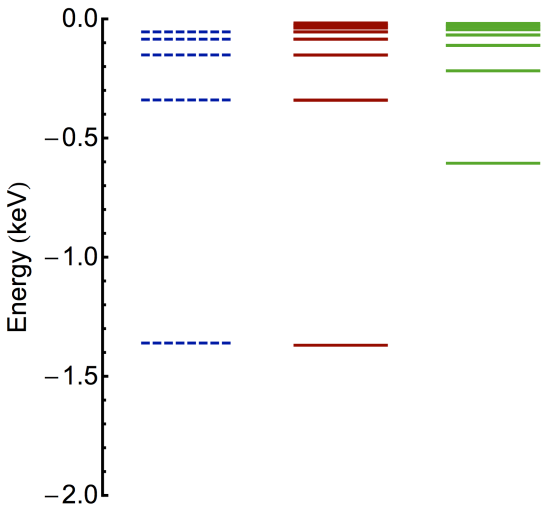

FIG. 3: Energy levels according to spherical Schrödinger theory (blue dashed), spherical Klein-Gordon theory (red), and cylindrical Klein-Gordon theory (green) for hydrogen-like neon with $B_0 = 0$.

and the eigenfunctions are

$$R(\rho) = F(-n_r, 2(b+1), 2k\rho)\rho^b e^{-k\rho} \tag{10}$$

where $b = \pm\sqrt{\ell_z^2 - Q^2q^2}$. Evidently for cylindrical hydrogenic ions, there are no solutions with $\ell_z = 0$ for any Z. A comparison of the energy levels for cylindrical and spherical neon is shown in Fig. 3.

B. Numerical Solutions for Soft Core Potentials

In numerical problems, the Coulomb potential can only be approximated due the singularity at the origin. Typically one replaces the Coulomb potential with a "soft-core potential," which for cylindrical atoms has the form

$$\Phi = \frac{Q}{\sqrt{\delta\rho^2 + \rho^2}} \tag{11}$$

Obviously, as $\delta\rho \to 0$ the soft-core potential becomes a Coulomb potential. In order to solve the nonlinear eigenvalue problem (5) with a soft-core potential, a numerical scheme has to be employed. Due to the quadratic form of the nonlinearity, the system can be reduced to a linear problem of twice the size [17]. In particular, let $R(\rho)$ be discretized on a sequence

of mesh points $\{\rho_i = (2i-1)\frac{\Delta\rho}{2} | i \in \mathbb{N}\}$. Evaluating the Laplacian operator in (5) by finite volumes gives the block tridiagonal matrix equation

$$\begin{pmatrix} 0 & 1 \\ -T & -D \end{pmatrix} \begin{pmatrix} R \\ R' \end{pmatrix} = \omega \begin{pmatrix} R \\ R' \end{pmatrix} \tag{12}$$

where $R = (R_0, R_1, R_2, \ldots)$, $R_i = R(\rho_i)$, $R' = \omega R$, T is a tridiagonal matrix, and D is a diagonal matrix. The non-zero elements of T and D are

$$T_{i,i-1} = \frac{\rho_i - \Delta\rho/2}{\rho_i \Delta\rho^2} \tag{13a}$$

$$T_{i,i} = q^2\Phi_i^2 - m^2 - \frac{\ell_z^2}{\rho_i^2} - \frac{2}{\Delta\rho^2} + \ell_z q B_0 - \left(\frac{1}{2} q B_0 \rho_i\right)^2 \tag{13b}$$

$$T_{i,i+1} = \frac{\rho_i + \Delta\rho/2}{\rho_i \Delta\rho^2} \tag{13c}$$

$$D_{i,i} = -2q\Phi_i \tag{13d}$$

where $\Phi_i = \Phi(\rho_i)$. Standard sparse matrix packages can solve this system for various subsets of the eigenvalue-eigenvector pairs. A similar system can be constructed for spherical atoms.

One important difference between the bound states of a soft-core potential compared with those of a Coulomb potential is that a solution exists for $\ell_z = 0$ in the former case, but not the latter. This is illustrated in Fig. 4, which plots the $n_r = 0$ energy for $\ell_z = 0$ and $\ell_z = 1$ as a function of the soft-core radius, $\delta\rho$. The $\ell_z = 1$ energy is insensitive to $\delta\rho$, while the $\ell_z = 0$ energy exhibits singular behavior as $\delta\rho \to 0$. Of course, the energy of the discretized system does not actually diverge, even when $\delta\rho = 0$, due to the fact that the grid is constructed so that the point $\rho = 0$ is never sampled.

A discussion of divergent energies in a Coulomb potential can be found in Ref. [13].

C. Scalar Zeeman Effect

Numerical solution of the nonlinear eigenvalue problem (12) allows one to characterize the splitting of the energy levels of high-Z ions in extreme magnetic fields for scalar wavefunctions. Consider hydrogen-like cylindrical ununoctium (Z=118, the heaviest known element).

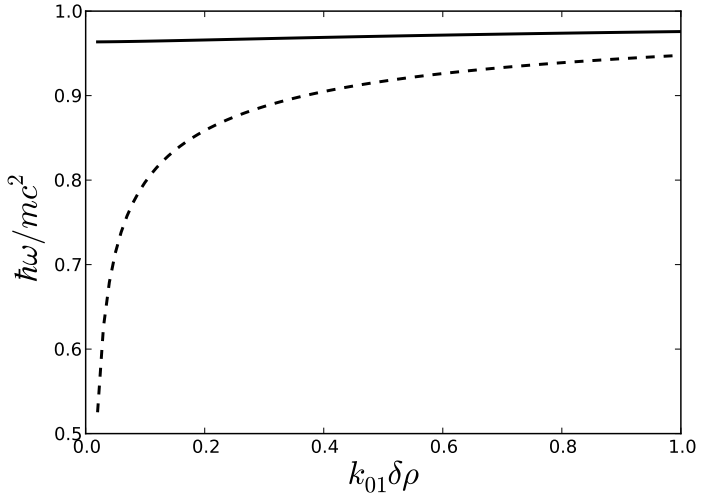

FIG. 4: Two lowest cylindrical bound state energies with $Z = 54$ as a function of soft core radius, $\delta\rho$. Dashed curve is $\omega_{00} = \omega(n_r = 0, \ell_z = 0)$ and solid curve is ω_{01}. The quantity $k_{01} = \sqrt{m^2c^2/\hbar^2 - \omega_{01}^2/c^2}$ characterizes the size of the ion (see Eq. 10).

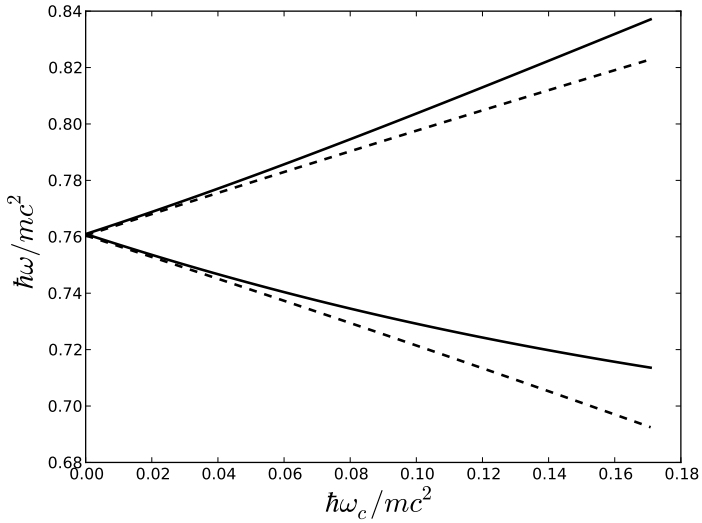

FIG. 5: Weak field (dashed) and numerical (solid) solution for energy levels in hydrogen-like ununoctium ($Z = 118$) with $\ell_z = 1$ (upper branches) and $\ell_z = -1$ (lower branches).

For the numerical calculation, the number of mesh points used is 2^{13}, while the mesh spacing and soft-core radius are $k_0\delta\rho = k_0\Delta\rho = 0.00125$, where $k_0 = k(\omega_c = 0)$. A comparison of the numerical solution and the weak-field solution is shown in Fig. 5. The characteristic size

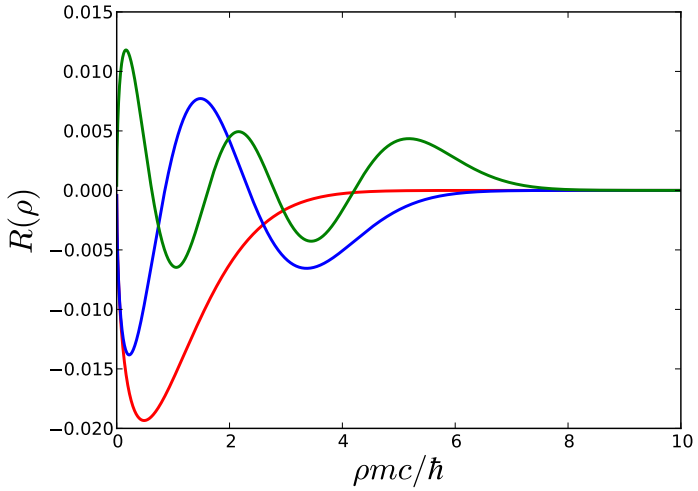

FIG. 6: Radial eigenfunctions in a strong field ($B_0 = 10$) for $n_r = 0$ (red), $n_r = 2$ (blue), and $n_r = 4$ (green), with $Z = 118$ and $\ell_z = 1$.

of the ununoctium ion is $1/k \approx 1.5$, so that the weak field limit corresponds to $\omega_c \ll 0.44$. Inspection of Fig. 5 shows that if ω_c is an order of magnitude below the weak field cutoff, the two solutions agree. At larger fields, the weak field solution underestimates the shift for the upper branch, and overestimates it for the lower branch. A few radial eigenfunctions in a strong field are shown in Fig. 6.

In ordinary units, the weak field cutoff of $\omega_c = 0.44$ corresponds to $B_0 \approx 20$ TG, with the peculiar result that $B_0 = 1$ TG is a weak field. At present, such fields are observed only in connection with astrophysical phenomena [14]. The highest laboratory fields to date are laser generated, and are still limited to hundreds of MG [15]. Our primary interest here is in code validation, i.e., establishing results that can be compared with the fully time-dependent calculations discussed below.

In the strong field limit, one can make progress analytically by means of the quasi-classical approximation. Defining $u(\rho) = R(\rho)\rho^{1/2}$, the eigenvalue problem takes the form of a one dimensional Schrödinger equation

$$u'' + 2\left[\epsilon(\omega) - U(\omega,\rho)\right] u = 0 \tag{14}$$

where the effective energy eigenvalue is $\epsilon(\omega) = \omega^2/2 - \ell_z m\omega_c/2 - m^2/2$ and the effective potential is

$$U(\omega,\rho) = -\frac{\omega Q q}{\rho} + \frac{b^2 - 1/4}{2\rho^2} + \frac{1}{8}\omega_c^2\rho^2 \tag{15}$$

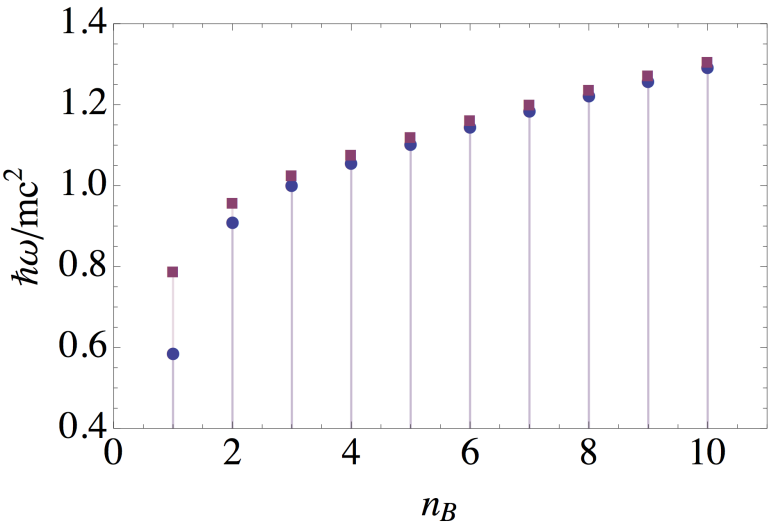

FIG. 7: Comparison of Bohr-Sommerfeld energy levels (circles) with solution of discretized eigensystem (squares), for $B_0 = 0.5$, $\ell_z = 1$, and $Z = 118$.

For states with $n_r \gg 1$ or $\ell_z \gg 1$ (equivalently, $\omega \to m$), Bohr-Sommerfeld quantization may be employed. The quantization rule is

$$\int_{\rho_1}^{\rho_2} d\rho \sqrt{2\left[\epsilon(\omega) - U(\omega,\rho)\right]} = \left(n_B + \frac{1}{2}\right)\pi \tag{16}$$

where $n_B + 1 \in \mathbb{N}$, and ρ_1 and ρ_2 are roots of the integrand. We associate the Bohr-Sommerfeld quantum number, n_B, with the radial quantum number, n_r. Fig. 7 compares the energy levels for $B_0 = 0.5$, $\ell_z = 1$, and $Z = 118$, as computed using Bohr-Sommerfeld quantization and direct numerical solution of the eigensystem (12). As expected, the agreement improves for higher quantum numbers. The error asymptotes to a finite value due to discretization errors in the solution of (12). Fig. 8 shows a similar comparison for several values of the magnetic field, holding n_B fixed at $n_B = 10$. For the highest value of the magnetic field, the solutions for several values of ℓ_z are displayed.

IV. TIME DEPENDENT SIMULATIONS

A. Numerical Algorithm

The Klein-Gordon equation is a second order hyperbolic equation. It can be explicitly differenced, provided a Courant-type condition is satisfied. Centered time differencing of

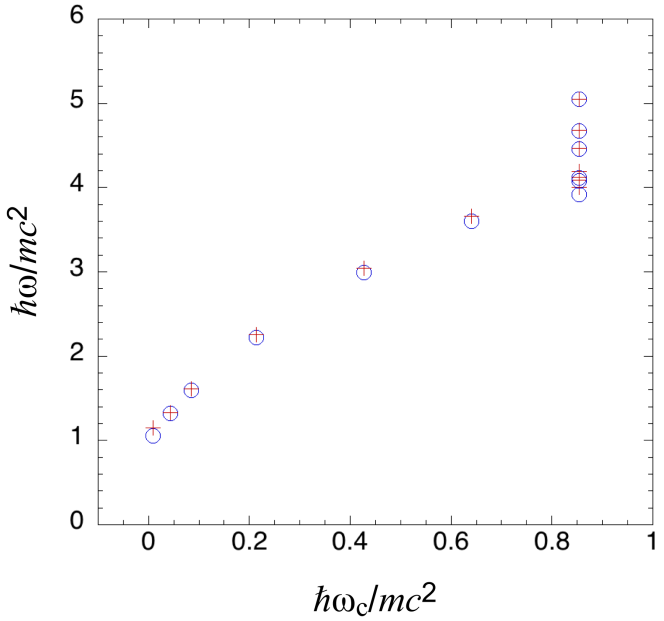

FIG. 8: Comparison of Bohr-Sommerfeld energy levels (circles) with solution of discretized eigensystem (plus signs) as a function of magnetic field, for $n_B = 10$, $\ell_z = 1$, and $Z = 118$. For the highest value of ω_c, solutions are plotted for $-3 \leq \ell_z \leq 3$

Eq. (3), with $\partial_t \Phi = 0$, gives

$$\frac{\Psi^{n+1}}{\Delta t^2} = \frac{(\nabla^2 + q^2\Phi^2 - q^2 A^{n2} - m^2)\Psi^n - 2i\nabla\cdot(q\mathbf{A}^n\Psi^n)}{1 + iq\Phi\Delta t} + \frac{2\Psi^n - (1 - iq\Phi\Delta t)\Psi^{n-1}}{\Delta t^2(1 + iq\Phi\Delta t)} \tag{17}$$

where n indexes the time levels. The spatial derivatives can be put in finite difference form by means of finite volumes. On a two-dimensional Cartesian grid, this results in

$$\nabla^2\Psi^n_{i,j} = \frac{\Psi^n_{i-1,j} - 2\Psi^n_{i,j} + \Psi^n_{i+1,j}}{\Delta x^2} + \frac{\Psi^n_{i,j-1} - 2\Psi^n_{i,j} + \Psi^n_{i,j+1}}{\Delta y^2} \tag{18a}$$

$$\nabla\cdot(\mathbf{A}^n_{i,j}\Psi^n_{i,j}) = \frac{\mathbf{A}_{i+1,j}\Psi^n_{i+1,j} - \mathbf{A}_{i-1,j}\Psi^n_{i-1,j}}{2\Delta x} + \frac{\mathbf{A}_{i,j+1}\Psi^n_{i,j+1} - \mathbf{A}_{i,j-1}\Psi^n_{i,j-1}}{2\Delta y} \tag{18b}$$

where i and j index the mesh points. The extension to three dimensions is straightforward. The numerical properties of this scheme can be evaluated by inserting the form $\Psi^n_{i,j,k} = \exp[\imath(ip_x\Delta x + jp_y\Delta y + kp_z\Delta z - n\omega\Delta t)]$ into the difference equations, with a constant, uniform $\mathbf{A}$ and Φ. The resulting numerical dispersion relation is

$$\sin^2\left(\frac{\omega\Delta t}{2}\right) = F(\mathbf{p}) + G(\omega) + \frac{1}{4}\Delta t^2\left(m^2 + q^2A^2 - q^2\Phi^2\right) \tag{19}$$

where

$$F(\mathbf{p}) = \sum_i \left[\frac{\Delta t^2}{\Delta_i^2} \sin^2(p_i \Delta_i/2) - \frac{\Delta t^2}{2\Delta_i} q A_i \sin(p_i \Delta_i) \right] \tag{20a}$$

$$G(\omega) = \frac{1}{2} \Delta t q \Phi \sin(\omega \Delta t) \tag{20b}$$

In the equation for $F(\mathbf{p})$, i indexes Cartesian coordinates, with $\Delta_1 = \Delta x$, etc.. It is easily verified that in the limit where the arguments of the trigonometric functions are small, the numerical dispersion relation reduces to the true dispersion relation,

$$(\omega - q\Phi)^2 = (\mathbf{p} - q\mathbf{A})^2 + m^2 \tag{21}$$

For a free particle, $A = \Phi = 0$, and the energy will always be real provided

$$\frac{1}{\Delta t^2} > \left(\frac{1}{\Delta x^2} + \frac{1}{\Delta y^2} + \frac{1}{\Delta z^2} \right) + \frac{m^2}{4} \tag{22}$$

In one dimension, this becomes $\Delta t < \Delta z (1 + m^2 \Delta z^2/4)^{-1/2}$. Note that if the cell size is much smaller than the Compton wavelength of the particle in question ($\Delta z \ll 1/m$), then the familiar Courant condition for the wave equation is recovered. A more general stability criterion is $0 < \mathcal{M} < 1$, where

$$\mathcal{M} = F(\mathbf{p}) + G(\omega) + \frac{1}{4} \Delta t^2 (m^2 + q^2 A^2 - q^2 \Phi^2) \tag{23}$$

Here, unlike the case of a free particle, instabilities can occur either in the large or small momentum limits. This is because even when $\mathbf{p} \to 0$, a large Φ can still drive $\mathcal{M}$ negative. The one-dimensional numerical dispersion relation for $q\Phi = -10$ and $qA = 0$ is shown in Fig. 9. Discretization parameters leading to instability give Fig. 9(a), while parameters leading to stability give Fig. 9(b).

B. Validation Against Zeeman Effect

Two codes have been written that implement the above algorithm on General Purpose Graphical Processing Units (GPGPU). One is programmed using Python and OpenCL, and the other is a turboWAVE module programmed using C++ and OpenCL. The turboWAVE version supports combined Message Passing Interface (MPI) and GPGPU programming. It is fully three dimensional, although the examples treated here are two-dimensional.

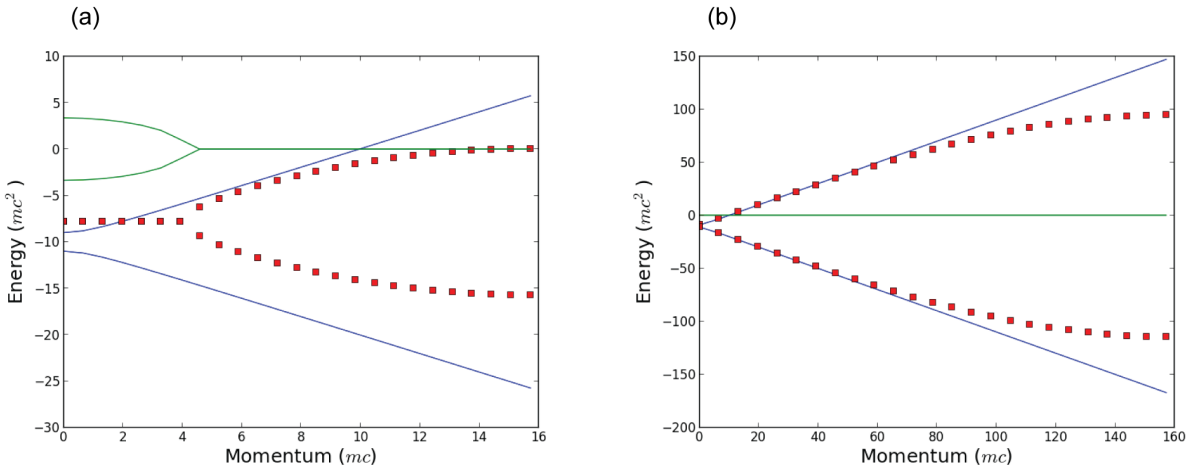

FIG. 9: Numerical vs. actual dispersion relation with $q\Phi = -10$ and $qA = 0$. Blue curves are the true energy, red squares are the real part of the numerical energy, and green curves are the imaginary part of numerical energy. Panel (a) is for $\Delta z = 0.2$ and $\Delta t = 0.1$, while panel (b) is for $\Delta z = 0.02$ and $\Delta t = 0.01$.

In order to validate the two codes, they are benchmarked against time independent calculations of relativistic Zeeman splitting. In order to extract the spectrum of stationary states from a time dependent code, it is desirable to use an initial condition that is a superposition of all possible states. At the same time, the results should not be prejudiced by the initial condition. An entirely random initial wavefunction serves both purposes. After allowing this wavefunction to evolve for a suitably long time, the spectrum can be estimated by Fourier transformation in time at selected points in space. The spectrum at each spatial point is different in terms of the relative magnitude of the spectral lines, but the energy of each line is independent of the spatial point chosen.

Two simulations are performed, one with $B_0 = 0$ and one with $B_0 = 0.5$. The binding potential is a cylindrical soft-core potential, with $Z = 118$ and $\delta\rho = 0.2$. The grid contains 8000×8000 cells, with cell size 0.02×0.02. The time step is 0.01 and 9×10^5 steps are taken. The results for $B_0 = 0$ and $B_0 = 0.5$ are shown in Fig. 10. The solid curves in the form of discrete peaks are the Fourier transformed wavefunction at two different spatial points. As expected, the height of the peaks depends on the spatial point, but the energy does not. The energies are also determined by solving the time independent system (12) for various values of n_r and ℓ_z. These solutions are shown as vertical dashed lines. Except for the highest lying bound states in the $B_0 = 0$ case, the two calculations agree. Actually, a

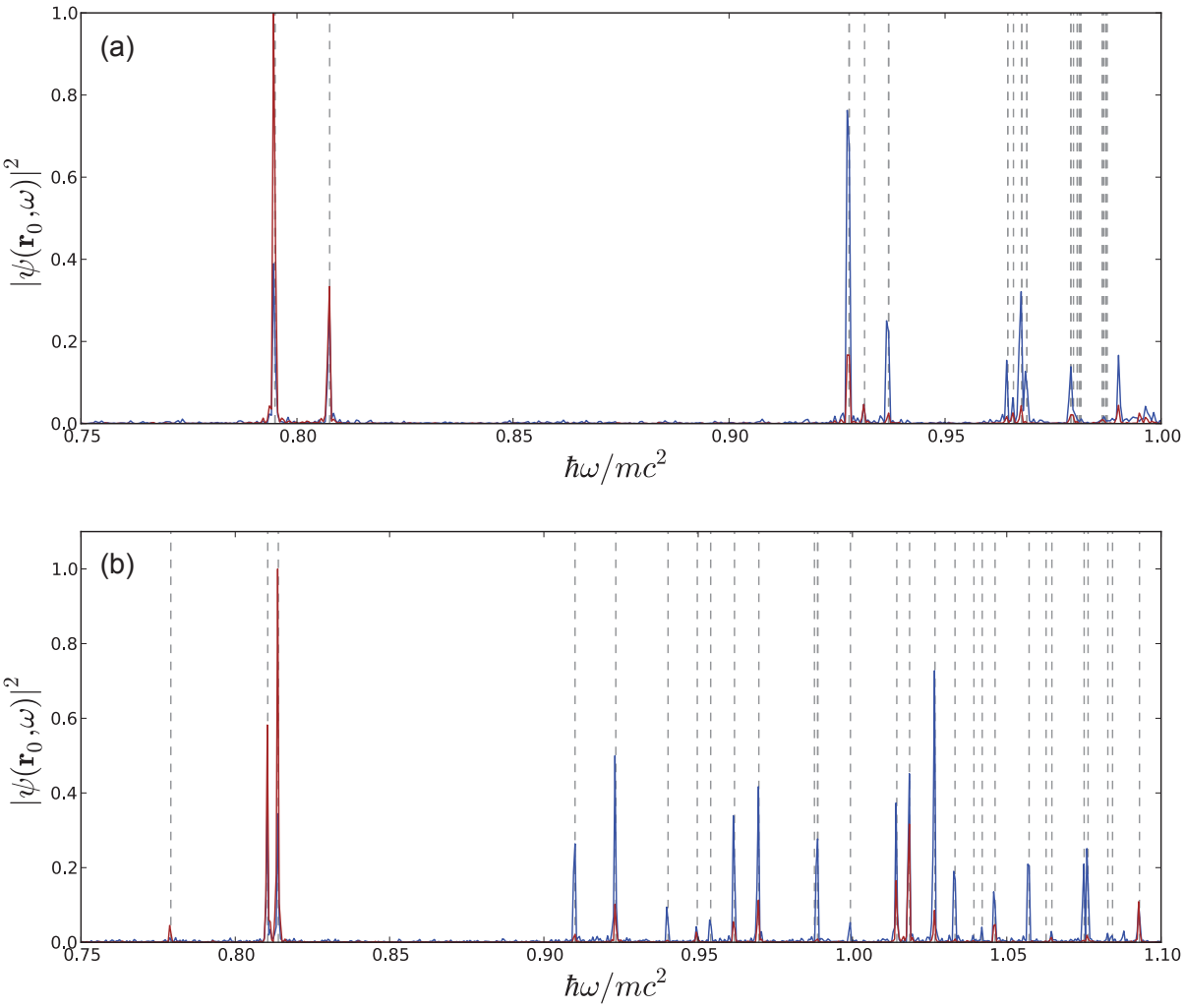

FIG. 10: Comparison of energy levels in a cylindrical soft core potential with $Z = 118$, with (a) $B_0 = 0$, and (b) $B_0 = 0.5$, as determined by time dependent (solid) and time independent (dashed) calculations. The brown lines are the Fourier spectrum evaluated at $\mathbf{r}_0 = 2\mathbf{e}_x$ and the blue lines are the Fourier spectrum evaluated at $\mathbf{r}_0 = 5\mathbf{e}_x$. The blue spectrum is multiplied by four.

real ion has an unbounded density of states as $\omega \to 1$ when $B_0 = 0$, whereas any numerical ion has only a finite number of states. It should also be noted that in a magnetic field, the bound state spectrum is not bounded from above, i.e., bound states exist for $\omega > 1$.

TABLE II: Parameters for simulation of relativistic ionization

Parameter	Symbol	Value
Steps	N_t	200000
Time Step	Δt	$0.2\hbar/mc^2$
Cells	$N_x \times N_y$	4000×12000
Space Step	$\Delta x, \Delta y$	$\hbar/mc$
Residual Charge	Q	$18\alpha^{1/2}$
Soft Core Radius	$\delta\rho$	$\hbar/mc$
Radial Quantum Number	n_r	0
Magnetic Quantum Number	ℓ_z	1
Laser wavelength	λ	24 nm
Vector Potential	a_0	3.3

C. Relativistic Ionization Example

Relativistic photo-ionization experiments will likely involve laser radiation at a wavelength of $\lambda = 0.8$ or $\lambda = 1.05$ μm. In order to model one cycle of the radiation, the number of time steps has to satisfy $N_t \gg \lambda/\lambda_c \approx 10^5$, where λ_c is the Compton wavelength. The number of grid cells in one dimension has to satisfy the same inequality due to the fact that the spatial scale of the orbit of a classical electron in a plane wave is λ in the relativistic limit. Based on the performance characteristics given below, a single GPGPU would take about 10^6 hours to complete such a calculation, even in two dimensions (assuming it had large enough memory). As a result, thousands of GPGPU compute nodes would be required to simulate a relativistic photo-ionization experiment at full scale.

In order to run an example on the currently available GPGPU cluster "Dirac" at the National Energy Research Supercomputing Center (NERSC), the parameters displayed in Table II are used. The simulation runs in about 1.2 hours. The primary scale reduction is the fictitious laser wavelength of 24 nm. The increased laser frequency means that fewer steps and grid cells have to be used to model a full cycle of the electron motion. The laser field has the form

$$\mathbf{A}(z,t) = a_0 \left[\cos(\omega_L z - \omega_L t) - 1\right] \Theta\left(t - z\right) \mathbf{e}_y \tag{24}$$

where Θ is the Heaviside step function. The electrostatic field is a soft core potential. The value of $a_0 = 3.3$ is determined by calculating the barrier suppression threshold [1] for an ion with residual charge $18\alpha^{1/2}$ (cylindrical H-like argon) and ground state energy 0.9961. The ground state energy is determined from Eq. (9) with $n_r = 0$ and $\ell_z = 1$, and corresponds to an ionization potential of about 2 keV. An interesting question is how well the barrier suppression model, which is based on electrostatic arguments, works in the relativistic limit.

The simulated ionization rate is defined in terms of the charge current flowing out of a volume containing the bound state. The Klein-Gordon equation satisfies the continuity equation $\partial_t \varrho + \nabla \cdot \mathbf{j} = 0$, where

$$\varrho = \frac{\imath q}{2m} \left(\Psi^* \partial_t \Psi - \Psi \partial_t \Psi^* \right) - \frac{q^2 \Phi}{m} \left| \Psi \right|^2 \tag{25}$$

is the analog of the classical charge density and

$$\mathbf{j} = -\frac{\imath q}{2m} \left(\Psi^* \nabla \Psi - \Psi \nabla \Psi^* \right) - \frac{q^2 \mathbf{A}}{m} \left| \Psi \right|^2 \tag{26}$$

is the analog of the classical current density. The expectation value of the charge contained in a ball $\mathcal{B}$ is

$$\langle q \rangle_{\mathcal{B}} = \int_{\mathcal{B}} d^3\mathbf{r} \varrho \tag{27}$$

Take the radius of $\mathcal{B}$ to be large enough so that it contains the charge associated with the bound state almost entirely. Then the ionization probability is defined as the expectation value of the charge outside $\mathcal{B}$, divided by the total charge of the particle:

$$P = \frac{q - \langle q \rangle_{\mathcal{B}}}{q} \tag{28}$$

The ionization rate is

$$W = \frac{dP}{dt} = -\frac{1}{q} \frac{\partial}{\partial t} \int_{\mathcal{B}} d^3\mathbf{r} \varrho \tag{29}$$

which by the divergence theorem, is the same as the current flowing out of the volume, divided by the charge. It should be noted that, due to the fact that ϱ can take either sign, this definition can lead to negative ionization probabilities. If the system being considered is an ordinary ion, one may interpret $P < 0$ as an indication that finding a positron outside of $\mathcal{B}$ is more likely than finding an electron. An intriguing possibility is that the laser field produces a free positron and an *additional* bound electron.

The ionization rate as defined above is displayed in Fig. 11(a). The applied electric field is displayed in Fig. 11(b). Some of the characteristics of the ionization rate are familiar from

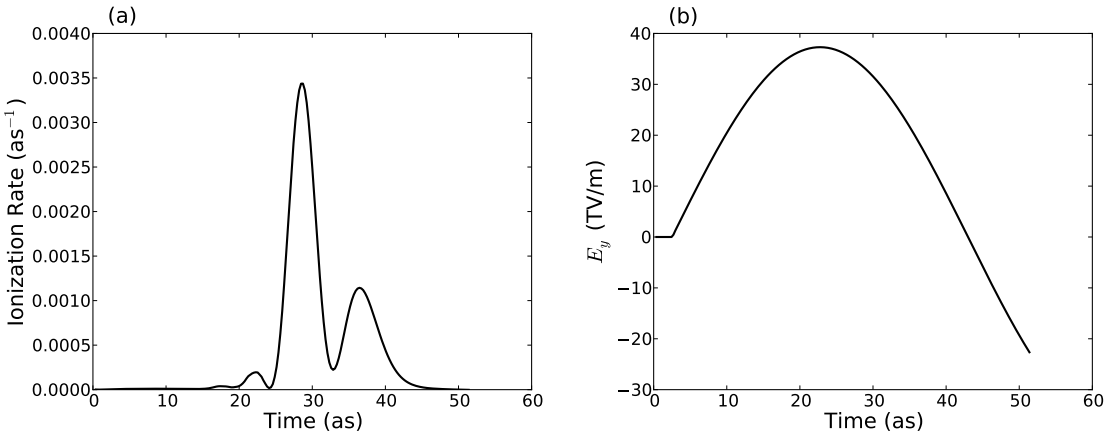

FIG. 11: Simulation of relativistic photo-ionization. (a) Rate defined as in (29) where $\mathcal{B}$ is a cylinder of radius 2.3 Å, (b) Applied electric field.

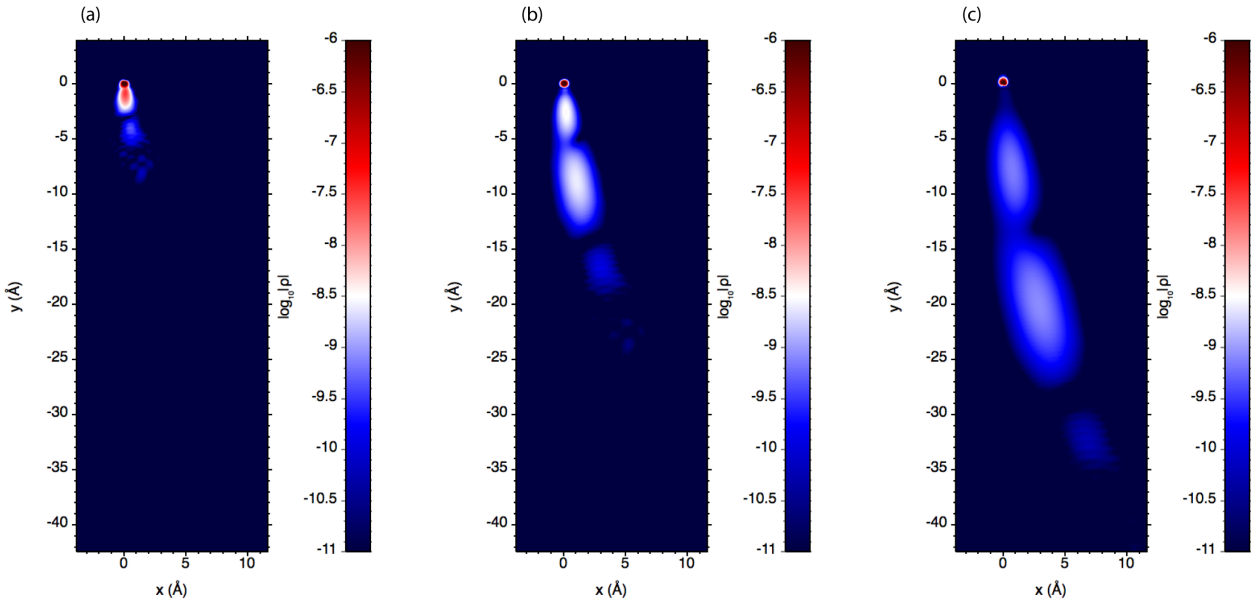

FIG. 12: Charge density associated with ionizing relativistic wavefunction evaluated at (a) $t = 26$ as (b) $t = 39$ as (c) $t = 52$ as.

the non-relativistic tunneling theory. First, the total ionization probability (area under the rate curve) is in the range of a few percent, so that the threshold field from [1] does indeed serve as a suitable threshold for ionization. Moreover, the peak of the ionization rate occurs near the peak of the electric field, as ordinary tunneling theory predicts. An unexpected feature is that the ionization rate has multiple peaks within one half-cycle of the applied field.

In order to visualize the relativistic ionizing wavefunction, the charge density, ϱ, is plotted as a false-color image in Fig. 12. The three panels show ϱ evaluated at three different times. The three peaks visible in the ionization rate correspond to the white and blue islands visible against the dark background in Figs. 12(b) and (c). The remnant of the bound state is the dark red feature at $(x, y) = (0, 0)$. One can clearly see a feature of the Volkov solution for an electron in a plane wave. Namely, the wavefunction is bent in the direction of the electromagnetic wave propagation. One would like to characterize how this "ponderomotive" effect alters the recollision phenomena that are well known in the non-relativistic case.

V. COMPUTATIONAL PERFORMANCE

As discussed above, the fundamental scale ratio in a relativistic quantum optics problem is λ/λ_c, where λ is the laser wavelength and λ_c is the Compton wavelength. Due to the large order of magnitude of this ratio, computational performance is crucial. To this end, we developed a relativistic quantum optics module within the turboWAVE framework [18]. Among other things, turboWAVE provides a programming environment for solving partial differential equations on various structured grids. The framework provides abstractions that are useful for parallelization. Parallelization across distributed processors is accomplished via the Message Passing Interface (MPI). Parallelization across shared memory processors is accomplished via the OpenCL language. In the latter case, particular attention is given to general purpose graphical processing units (GPGPU).

Parallelization of the Klein-Gordon equation is accomplished via domain decomposition, where each GPGPU advances the solution in a given domain, and MPI is used for communication between domains. The structure of a two-dimensional domain is shown in Fig. 13 (the extension to three dimensions is straightforward, and has been implemented in turboWAVE). Cells are labeled either by an index space pair, which correspond to a spatial location, or a single index that corresponds to a location in computer memory. The region of memory where the domain resides is called the compute buffer. In the figure, the white layer of cells are ghost cells, the blue cells are edge cells, and the orange cells are interior cells. The ghost cells and edge cells together are called boundary cells. The interior and edge cells can be updated independently on each domain provided the ghost cells contain the values of the edge cells in adjacent domains. The problem of parallelizing the solution,

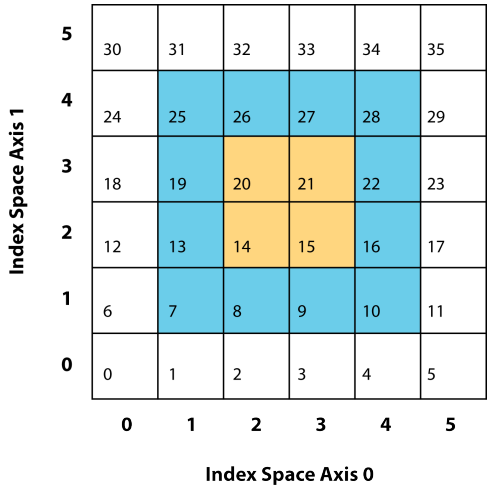

FIG. 13: Structure of a typical computational domain. The index space axes correspond directly to physical axes in space, while the indices written in each cell correspond to a location in memory.

then, reduces to that of updating the ghost cells in the memory of a given GPGPU using information from other GPGPUs. An efficient realization of this operation is outlined as follows:

1. Device: Copy boundary cells from compute buffer into a contiguous transfer buffer
2. Device: Copy transfer buffer to host memory
3. Host: Update ghost cells using MPI as usual
4. Device: Read updated transfer buffer from host memory
5. Device: Copy cells from transfer buffer to compute buffer

Here, the OpenCL terminology "device" and "host," typically refers to a GPGPU and CPU, respectively. Operations with the transfer buffer are facilitated by storing an index map on the GPGPU. The index map contains pairs of indices, where one index in the pair points to a location in the compute buffer, and the other points to the corresponding location in the transfer buffer.

Once the ghost cells have been updated, the GPGPU can advance the relativistic wave-function using the Klein-Gordon equation. This requires that the compute buffer contain Ψ^{n-1}, Ψ^{n}, and A^{n}_{μ} [19]. In cases where the potential is time varying, an efficient way of updating it is required. In order to avoid calling special functions on the GPGPU, both the

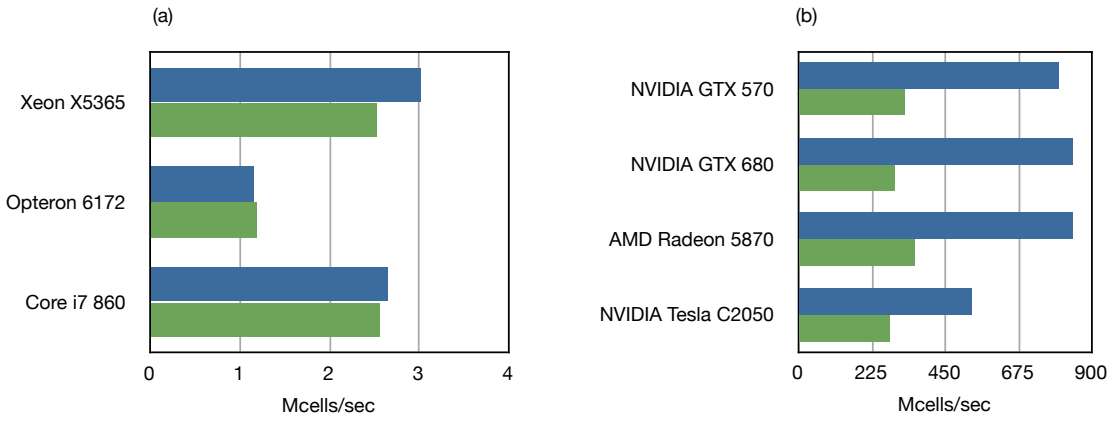

FIG. 14: Performance in terms of millions of cells (Mcells) per second for various (a) CPU cores and (b) GPGPUs. Blue bars are for single precision and green bars are for double precision.

Python code and turboWAVE assume **A** is in the form of a plane wave. The host updates a single longitudinal strip, which is then copied to a device buffer. The GPGPU then duplicates the strip at every transverse index. The Klein-Gordon update, as described in section IV A, is then executed. Each cell in the compute buffer is an OpenCL work item. Since the algorithm involves no spatial derivatives of Ψ^{n-1}, it can be carried out in place by storing Ψ^{n+1} in the memory occupied by Ψ^{n-1}.

The performance of the algorithm on a single compute node (no network message passing) is illustrated in Fig. 14 for several CPU and GPGPU devices. One notable characteristic is that the single and double precision performance is nearly the same on a CPU, but differs by more than two-fold on a GPGPU. In terms of double precision performance, a GPGPU is typically 100 times faster than a single CPU core. In the most extreme case, the NVIDIA GTX 680 running in single precision mode is over 700 times faster than one core of the Opteron 6172 "Magny-Cours." The floating point efficiency (sustained to peak throughput) ranges between 4% and 10% for both CPU cores and GPGPUs.

Finally, Fig. 15 shows the results of a scaling study carried out on the GPGPU cluster "Dirac" at the National Energy Research Supercomputing Center (NERSC). The study was carried out up to the maximum number of GPGPU nodes that are made available by the queuing system. Fig. 15(a) shows the performance in the aggregate vs. the number of MPI compute nodes, where each node is assigned a single GPGPU. The results are shown for three different size grids. The results normalized to the number of GPGPUs are shown in

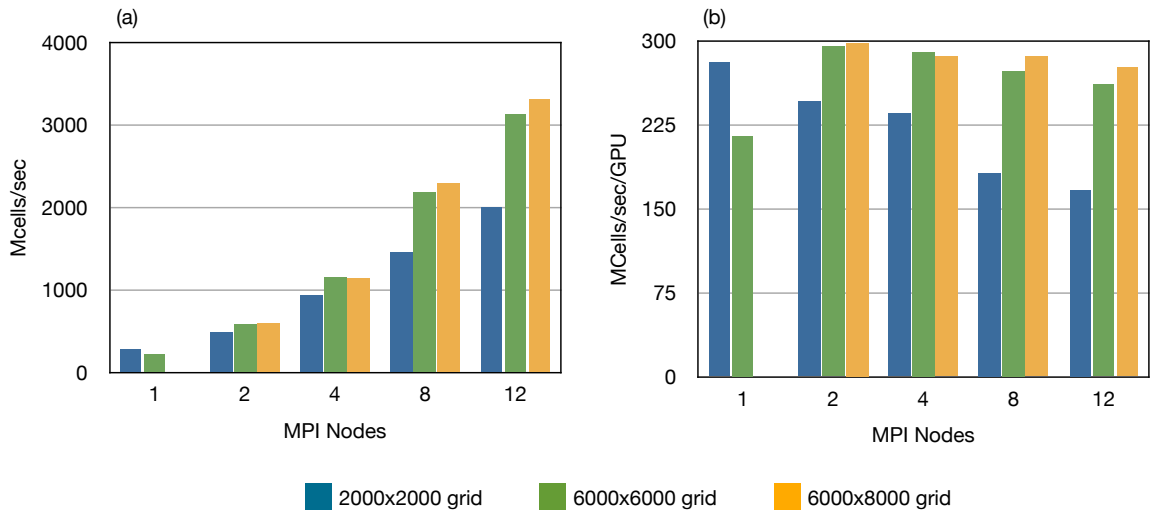

FIG. 15: Scaling study on NERSC GPGPU cluster "Dirac" for three different size grids showing (a) millions of cells per second in the aggregate, and (b) millions of cells per second on each GPGPU. Double precision is used in all cases. One GPGPU is assigned to each MPI node.

Fig. 15(b). The performance per GPGPU on the smallest grid drops noticeably in going from 1 to 12 nodes. For the larger size grids, the performance is well sustained. An interesting feature is that the performance per GPGPU actually increases in going from 1 to 2 nodes on the medium grid. This may indicate there is a performance penalty incurred when the device memory is nearly exhausted. Note that for the large grid, the case of a single node could not be carried out due to reaching the device memory limit. In the best case each GPGPU achieves 45 GFLOPS per second, about 9% of the theoretical maximum. The best floating point performance in the aggregate is 0.5 TFLOPS per second.

VI. CONCLUSIONS

The availability of high performance computing resources makes it possible to carry out relativistic quantum optics calculations from first principles. A starting point is to solve the Klein-Gordon equation for a spin zero particle. Solutions of the time independent equation are developed analytically and numerically in order to initialize time dependent calculations. Energy levels extracted from the time dependent code are in agreement with those obtained from time independent calculations and analytical solutions. The time dependent calculation provides solutions to relativistic quantum optics problems such as relativistic

photo-ionization of high-Z ions by extreme fields. This type of calculation is made possible by modern heterogeneous computing resources, and opens up the little-explored field of relativistic quantum optics.

VII. ACKNOWLEDGEMENTS

This work was supported by the NRL 6.1 base program. We acknowledge Mr. Kevin Fung's assistance in developing the GPGPU programming expertise used in this work. The "Dirac" GPGPU cluster is a resource of the National Energy Research Scientific Computing Center (NERSC), which is supported by the Office of Science of the U.S. Department of Energy under Contract No. DE-AC02-05CH11231. Resources of the Department of Defense High Performance Computing and Modernization Program (HPCMP) were also used in this work.

[1] S. Augst, D. Strickland, D.D. Meyerhofer, S.L. Chin, and J.H. Eberly. Tunneling ionization of noble gases in a high-intensity laser field. *Phys. Rev. Lett.*, 63(20):2212–2215, Nov 1989.

[2] L. V. Keldysh. Ionization in the field of a strong electromagnetic wave. *Soviet Physics JETP*, 20(5):1307–14, May 1965.

[3] A.M. Perelemov, V.S. Popov, and M.V. Terent'ev. Ionization of atoms in an alternating electrical field. *Soviet Physics JETP*, 23(5):924–934, 1966.

[4] A.M. Perelemov, V.S. Popov, and M.V. Terent'ev. Ionization of atoms in an alternating electrical field. ii. *Soviet Physics JETP*, 24(1):207, 1967.

[5] A.M. Perelemov and V.S. Popov. Ionization of atoms in an alternating electrical field. iii. *Sov. Phys. JETP*, 25(2):336–343, Aug 1967.

[6] A.M. Perelemov, V.S. Popov, and V.P. Kuznetsov. Allowance for the Coulomb interaction in multiphoton ionization. *Soviet Physics JETP*, 27(3):451–457, 1968.

[7] V.P. Krainov and A.V. Sofronov. Landau-Dykhne approach for relativistic electron momentum and angular distributions for the ionization of multicharged atomic ions by superintense laser fields. *Phys. Rev. A*, 77:063418–1–063418–6, 2008.

[8] V.S. Popov. Tunnel and multiphoton ionization of atoms and ions in a strong laser field (Keldysh theory). *Physics-Uspekhi*, 47(9):855–885, 2004.

[9] V.P. Krainov and A.V. Sofronov. The Landau-Dykhne approach for relativistic electron energy spectra in the tunneling ionization of atoms by superintense linearly polarized radiation. *Ultrafast Opt. and Strong Field Phys.*, 14(3):401–403, 2004.

[10] M. Ruf, H. Bauke, and C.H. Keitel. A real space split operator method for the Klein-Gordon equation. *J. Comp. Phys.*, 228:9092–9106, 2009.

[11] H. Bauke and C.H. Keitel. Accelerating the Fourier split operator method via graphics processing units. *Computer Phys. Comm.*, 182:2454–2463, 2011.

[12] V.B. Berestetsky, E.M. Lifshitz, and L.P. Pitaevskii. *Quantum Electrodynamics*. Pergamon Press, 1980.

[13] L.D. Landau and E.M. Lifschitz. *Quantum Mechanics*. Pergamon Press, Oxford, England, 1980.

[14] F. Camilo, V.M. Kaspi, A.G. Lyne, R.N. Manchester, J.F. Bell, N. D'Amico, N.P.F. McKay,

and F. Crawford. Discovery of two high magnetic field radio pulsars. *The Astrophysical Journal*, 541:367–373, Sep 2000.

[15] M. Tatarakis, I. Watts, F.N. Beg, E.L. Clark, A.E. Dangor, A. Gopal, M.G. Haines, P.A. Norreys, U. Wagner, M.-S. Wei, M. Zepf, and K. Krushelnick. Measuring huge magnetic fields. *Nature*, 415:280, Jan 2002.

[16] It should be noted that a cylindrical Coulomb potential implies a nuclear charge that is distributed throughout all space

[17] This method of solution is well known, and can be found on the world wide web (see, e.g., Wikipedia)

[18] A separate Python version is also under development

[19] One could also save storage by computing A_μ^n during the advance of Ψ, but then special function calls might be needed.